COMMUNICATIONS PHYSICS

ARTICLE

https://doi.org/10.1038/s42005-020-0295-5 OPEN

Nonrelativistic electron–electron Møller scattering in a nonadiabatic tunnel-ionizing surface plasmon field

S.R. Greig[1]*, J.B. Khurgin[2] & A.Y. Elezzabi[1]

Ultrafast processes occurring on nanoscale surfaces can be probed with ultrafast low-energy electron pulses. Specifically, for metallic samples, the interaction of free electrons with surface plasmon fields provides insight into the nanoscale electron dynamics at the surface. Current models and experiments include the interaction of electrons with the sample, but ignore electron–electron and electron–plasmon interactions. Here we show that secondary electrons and their interaction with the incident primary electrons via nonrelativistic Møller scattering in the presence of optical and surface plasmon fields significantly alters the electron dynamics probed with ultrafast low-energy electron microscopy. Modeling this electron–plasmon interaction is key for interpreting ultrafast electron dynamics on metallic surfaces.

---

[1] Ultrafast Optics and Nanophotonics Laboratory, Department of Electrical and Computer Engineering, University of Alberta, Edmonton, AB T6G 1H9, Canada. [2] Department of Electrical and Computer Engineering, Johns Hopkins University, Baltimore, MD 21218, USA. *email: sgreig@ualberta.ca

Surface plasmons (SPs) are collective oscillations of charge density waves that can be optically driven at interfaces between materials having permittivities of the opposite sign. The nanoscale localization and steep spatial gradient of the SP field leads to enhanced electromagnetic field–matter interaction. On the fundamental level, free electron–electron interaction in the presence of SP fields provides a wealth of information on ultrafast processes occurring on nanoscale surfaces. As such, it is imperative to understand how a free electron interacts with such fields, as this is a precursor for many key experiments in ultrafast surface science. For example, ultrafast electron microscopy (UEM) has potential to resolve processes in nature with temporal resolution approaching the attosecond regime[1–5] and spatial resolution on the order of the atomic unit of length. Studying dynamics in matter at ultrahigh spatial and temporal resolution enables unprecedented insight into a wide range of topics including phase changes in materials[1,6–8], charge density waves on surfaces[9,10], chemical bonding dynamics[11–13], and structural surface dynamics[14,15]. A common approach to interpreting the electron dynamics probed in UEM relies on models for the electron–sample interaction, which tend to ignore interactions along the electron's trajectory inside the sample[16].

The large penetration depth of the high-energy electrons (50–200 keV) employed in most UEM setups limits these experiments to studying the bulk response of the material. However, on surfaces, probing such ultrafast dynamics requires electron interaction within a penetration depth of 1 nm that can only be achieved by low-energy electron pulses. Two low-energy candidates have emerged: ultrafast low-energy electron diffraction (ULEED) and high-resolution electron energy loss spectroscopy (HREELS). Although ULEED has demonstrated high surface sensitivity with ultrafast temporal resolution[10,17,18], its major limitation is that it is confined to probing structural dynamics and therefore is not effective for time-resolved studies of surface chemical reactions. On the other hand, studying surface chemical reactions requires the use of HREELS, which employs electron energies <100 eV and typically around 5 eV to achieve an energy resolution of 1 meV. Although HREELS provides surface chemical sensitivity, it does not reveal information about the important ultrafast temporal evolution of the reactions occurring at the surface. Extending the temporal resolution of time-resolved HREELS towards the attosecond timescale would prove indispensable for probing the time dynamics of a variety of surfaces[19–21] and studying various surface adsorbate reactions including carbon monoxide[22–24], molecular oxygen[25,26], water[27,28], aromatic compounds[29], and self-assembled monolayers[30,31]. Nonetheless, one has to understand first how an electron behaves in an SP field, especially when considering electron dynamics on metallic surfaces.

In a time-resolved, optical pump/electron-probe UEM experiment, a pulsed electron beam interacts with a sample at the same instant that it is being excited by an ultrafast laser pulse. In such arrangement, the probe electrons are influenced by the fields from the excitation optical pulse or, more importantly, the fields from the SP pulse excited by the aforementioned optical pulse. This interaction strength is significantly enhanced as the SP field strength approaches the strong field regime, where the ponderomotive energy of the SP field is comparable to the electron-binding energy. Although the interaction of SP fields and photoemitted electrons is well understood[32–37], the intimate dynamics of free, non-photoemitted, low-energy electrons interacting with SP fields are more fundamentally important, especially in the strong field interaction regime. The most important aspects of this SP–electron interaction that must be addressed are as follows: how these low-energy electrons interact with the SP field; how their kinetic energy and angular distribution will be affected; what happens when the SP field strength approaches the strong field regime; and the role of electron–electron scattering. Fully understanding this fundamental SP–electron interaction is a prelude for the advancement of low-energy, surface-sensitive UEM.

In this study, we investigate the interaction of high plasmonic fields and free electrons propagating nearly parallel to a metallic surface. We demonstrate that in the nonadiabatic tunnel-ionization regime (Keldysh parameter, γ, between 1 and 2), the existence of secondary electrons (SEs) and their interaction with primary electrons (PE) via Møller quantum mechanical non-relativistic scattering in the presence of optical and plasmonic fields play a major role in altering electron dynamics. The presence of SEs introduces a large population of low-energy electrons to the measured kinetic energy spectrum as well as significantly increasing the total number of electrons leaving the surface. This is particularly evident in UEM where the number of SEs is comparable to the number of PEs in the ultrafast electron-probe pulse. The angular distribution of the electrons is also skewed towards the direction of SP propagation with a distinct beaming of 25°–30°. All of these effects obscure information that is useful for both diffraction and electron energy loss experiments. The experimental results are confirmed via a detailed model that combines finite-difference time-domain (FDTD), Monte Carlo, and electron-tracking calculations.

Results

Experimental setup. The experimental setup used to study the interaction of free electrons with a plasmonic field is depicted schematically in Fig. 1. SPs having wavevector k_{SP} and peak electric field strength $|\mathbf{E}_{\mathrm{SP}}|$, are excited on a 45 nm Au film in the Kretschmann geometry by laser pulses from a Ti:Sapphire chirped pulse amplifier. The laser pulses have a duration of 50 fs and a central wavelength of 800 nm. The 5.7 mm-diameter laser spot size on the Au film ensures the largest possible electron–$\mathbf{E}_{\mathrm{SP}}$ interaction region in both space and time (see Supplementary Note 1 for calculation of the interaction region), while maintaining a Keldysh parameter between 1 and 2. A continuous PE beam from an electron gun is passed almost parallel to the Au film, along the same direction as k_{SP}. It is important to note that the PE beam has a

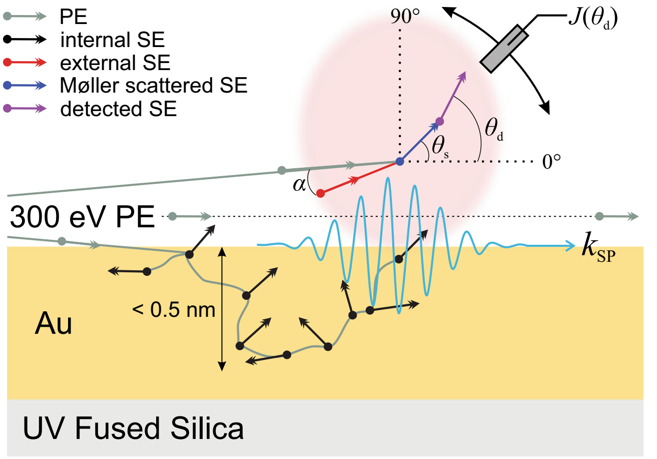

Fig. 1 Schematic depiction of experimental setup and relevant processes. Surface plasmons are excited on a 45 nm Au film. A 300 eV continuous primary electron (PE) beam propagates parallel to the Au film. Internal secondary electrons (SEs) are generated by PE collisions within 0.5 nm of the surface of the Au film. k_{SP} is the surface plasmon wavevector, α is the angle between PE and SE, θ_s is the Møller scattering angle, θ_d is the angle of the detected electrons, and J is the total collected current.

diameter of 2 mm and a 5° angular spread, such that a portion of PE collide with the Au film to generate SE. The kinetic energy of the PE beam is set to 300 eV and the beam current, I_{PE}, is varied as required. The PE kinetic energy of 300 eV is selected due to it being the experimentally determined peak for SE yield from Au films[38]. All electrons (PE, SE, and photoemitted electrons) are detected by a Faraday cup detector having an acceptance angle of 5°. The choice of a Faraday cup as a detector was dictated by its lack of perturbation to the PE beam compared with the high-voltage perturbation from more sensitive detectors, such as electron multipliers or channeltrons. The electron detector is placed on an angular translation stage so that the angular distribution of the electrons can be measured. Due to the placement and proximity of the electron gun to the sample, only angles between 0° and 90° can be measured. To only observe electrons (i.e., experiment electrons) that have interacted with the $\mathbf{E}_{\mathrm{SP}}$ or incident laser field, the output of the electron detector is connected through a low-noise current preamplifier to a lock-in amplifier that takes its reference from an optical chopper placed in the laser beam path.

Surface plasmon–free electron interaction. For surface-sensitive UEM, a key characteristic is the angular distribution of the electrons leaving the surface, especially for electron diffraction experiments. Therefore, it is important to investigate how the angular distribution changes in the presence of $\mathbf{E}_{\mathrm{SP}}$. Figure 2 depicts the angular distribution of the total measured current, J, as a function of I_{PE} at a fixed laser intensity, I_{laser}, of 25 GW cm^{-2}. At $I_{\mathrm{PE}} = 0$ nA, any detected electrons would be due to a plasmon-driven photoemission process from the Au film[33,34,39]. As expected, electron emission from the Au film peaks to 5.3 pA in a direction perpendicular to the film (with a total emission current of 37 pA) and has a half-width-at-half-maximum of 17.5° due to the ponderomotive force from $\mathbf{E}_{\mathrm{SP}}$ driving the photoemitted electrons in a direction away from the Au film. However, once the PE beam is introduced, even at currents as low as $I_{\mathrm{PE}} = 5$ nA, the situation becomes markedly different.

A noticeable difference with the presence of the continuous PE beam is the significant increase in J. At $I_{\mathrm{PE}} = 5$ nA, the total collected current is 309 pA, an 8.4× increase compared with $I_{\mathrm{PE}} = 0$ nA. Increasing I_{PE} to 50 and 500 nA results in total currents of 364 pA and 422 pA, respectively. The increase in J is accompanied with a distinct lobe centered at ~25°–30° away from the Au film. At $I_{\mathrm{PE}} = 5$ nA, the current peaks to 27.6 pA at 25°. At $I_{\mathrm{PE}} = 50$ nA and 500 nA, the lobe shifts to 30° and 35°, respectively. It is important to note that as the experiment uses phase-sensitive detection, only electrons that interact with the optical field or $\mathbf{E}_{\mathrm{SP}}$ are collected.

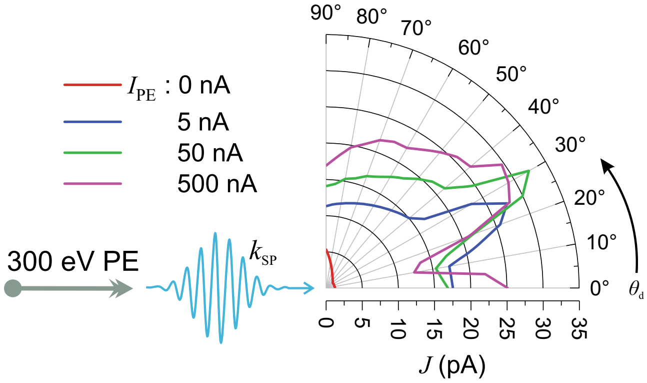

Fig. 2 Angular distribution of total measured current, *J*, at a fixed incident laser intensity, $I_{\mathrm{laser}} = 25$ GW cm^{-2}. Measured angular distribution at primary electron beam current, $I_{\mathrm{PE}} = 0$, 5, 50, and 500 nA.

To ascertain the origin of the increased J, it is imperative to determine the electron emission process, i.e., multi-plasmon photoemission, field emission, or tunnel ionization. Figure 3 depicts J as a function of I_{laser} at $I_{\mathrm{PE}} = 0$, 5, 50, and 500 nA. At $I_{\mathrm{PE}} = 0$ nA, a nonlinear power scaling dependence of 4.23 is observed (Fig. 3(a)). This is the standard four-plasmon emission process of electrons in the Au film absorbing four SP quantum with $h\nu = 1.55$ eV energy ($\lambda = 800$ nm) to overcome the Au work function, W_{F}, of 5.2 eV, confirming that with no PE present the electron emission process is strictly in the multi-plasmon absorption regime. Nevertheless, once PEs are introduced, the power scaling dependence changes. The total current scales linearly with the incident I_{laser} as depicted in Fig. 3b–d. It is well-known for plasmoemission (or photoemission) that the probability of a multi-plasmon process happening decreases significantly as the order of the process increases. As such, the lower (i.e., linear) emission order indicates that the previously observed multi-plasmon absorption process is suppressed in the presence of the PE beam. The change of slope between the three cases is

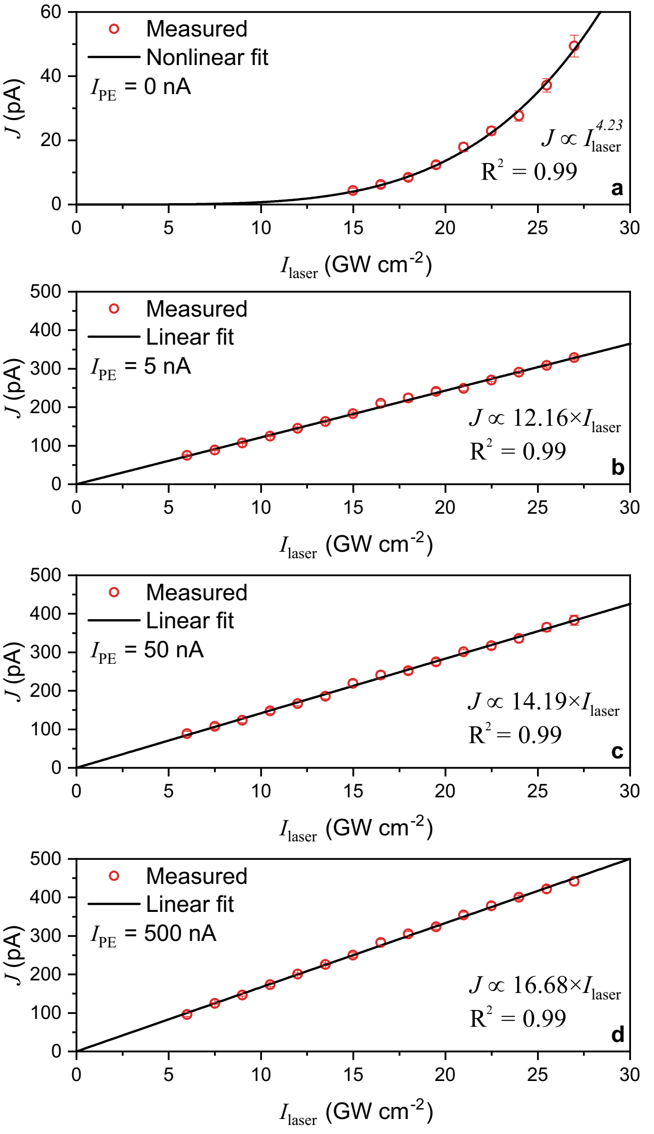

Fig. 3 Total measured current, *J*, as a function of incident laser intensity, I_{laser}. Power scaling dependence at primary electron beam current, $I_{\mathrm{PE}} =$ (**a**) 0 nA, (**b**) 5 nA, (**c**) 50 nA, and (**d**) 500 nA. The error bars represent the SD of *J*.

simply due to the increase in J as I_{PE} increases. The linear dependence and significant increase in J are indeed intriguing, indicating that a different process is responsible for the electron emission. It should be noted that electron beam induced image charges in the Au film affecting the emission process and the $\mathbf{E}_{\mathrm{SP}}$-driven ponderomotive force forcing electrons into collisions with the Au film do not manifest as a linear emission process (see Supplementary Notes 2 and 3 for electron-tracking simulations).

Clearly, the source of such electrons must be internal to the Au film. When an energetic PE inelastically collides with the outer shell electrons of the Au atoms, it may transfer some of its energy to these electrons, increasing their energy above the Fermi energy, E_{F}, to become internal SEs, which cannot gain energy from either the $\mathbf{E}_{\mathrm{SP}}$ field or the PE-induced image charge field (1.8×10^{-3} V nm^{-1}) over the PE penetration depth of <0.5 nm. However, if the PE beam transfers enough energy to the internal SE to overcome the surface potential barrier at the Au-vacuum interface, they will be ejected from the Au film to become external SEs (i.e., kinetic energies < 50 eV[40] and directed in a cosine distribution centered perpendicular to the material[41]). A key SE characteristic, which is important for the work presented here, is the SE yield, δ, or the fact that for a single PE it is possible to generate multiple SE via an avalanche process. For a 300 eV PE impinging on the Au film, $\delta = 1.14$[38]. Therefore, due to the 5° spread of the PE beam, a portion of the PE beam will collide with the Au film, generating SE that will subsequently interact with $\mathbf{E}_{\mathrm{SP}}$. However, δ does not vary with I_{PE} and therefore does not account for the observed linear emission process.

To shed light on the linear dependence, one must consider the SE emission process in the presence of $\mathbf{E}_{\mathrm{SP}}$. When the internal SE are generated within the Au film, they will have a range of kinetic energies, E_{i}, depending on the number and type of collisions they undergo in the Au film. Using the treatment by Kaneko[42] and the Lindhard potential[43,44], the internal SE kinetic energy spectrum can be calculated, as depicted in Fig. 4 (see Supplementary Note 4 for detailed calculations). It is noteworthy that the kinetic energy here is referenced to E_{F}, as the electrons are still residing within the material. Notably, 27% of the internal SE below the vacuum energy level, E_{vac}, (5.2 eV for the Au film) have energies within a single plasmon energy (1.55 eV) of E_{vac}, indicated by the shaded region in Fig. 4. Therefore, these internal SE are freed by absorbing a single SP quantum, as illustrated in the inset of Fig. 4. As this is a single-plasmon emission process, J scales linearly with I_{laser} and thus dictates the observed linear power scaling in Fig. 3b–d.

Just as the single-plasmon absorption of internal SE affects δ, it also modifies the kinetic energy spectrum of the detected electrons by producing a large population of low-energy (<1.55 eV) electrons that can be subsequently accelerated by $\mathbf{E}_{\mathrm{SP}}$. Figure 5 depicts the measured kinetic energy spectra at a fixed $I_{\mathrm{laser}} = 25$ GW cm^{-2} and at $I_{\mathrm{PE}} = 0$, 5, 50, and 500 nA. As expected, J is significantly increased when the PE are present. Although, for $I_{\mathrm{PE}} > 0$ nA, the shape of the kinetic energy spectra are quite similar, exhibiting a peak at 0 eV with a majority (i.e., ~60%) of their electrons having energies below 10 eV and a distinct hump around 20 eV. As the kinetic energy gained from acceleration by the $\mathbf{E}_{\mathrm{SP}}$ field is dependent on the residency time of the electron in the $\mathbf{E}_{\mathrm{SP}}$ field, the electron's final kinetic energy is highly dependent on the phase of $\mathbf{E}_{\mathrm{SP}}$ that they are born into. As such, the higher number of low-energy, <10 eV, electrons is ascribed to SE that have been freed from the Au film by single-plasmon absorption but do not experience the full acceleration of the $\mathbf{E}_{\mathrm{SP}}$ field. Remarkably, a portion of the SE is accelerated to higher kinetic energies, up to 35 eV, similar to those at $I_{\mathrm{PE}} = 0$ nA. As the kinetic energy gain from $\mathbf{E}_{\mathrm{SP}}$-driven acceleration is independent of the number of SE being excited, the shape of the kinetic energy spectrum does not change with I_{PE}, i.e., only the magnitude of J will vary with I_{PE}.

Monte Carlo simulations show that although the cosine angular distribution of the SE is slightly skewed along the direction of the PE beam, there is no evidence of directed SE beaming when the PE beam impinges on the Au surface at angles between 0° and 90° (see Supplementary Note 5). Notably, at the maximum $|\mathbf{E}_{\mathrm{SP}}|$ of the experiment (17 V nm^{-1}), the SEs retain their cosine angular distribution with no evidence of beaming (see Supplementary Note 5). Furthermore, at this $|\mathbf{E}_{\mathrm{SP}}|$, the ponderomotive force is not strong enough to deflect the 300 eV PE away from the surface of the Au film (see Supplementary Fig. 3). However, the external SE is a free electron that can interact with the plasmonic field via the ponderomotive force and with the incident 300 eV PE beam via electron–electron scattering.

PE–SE scattering in the presence of an $\mathbf{E}_{\mathrm{SP}}$ field can give rise to preferential beaming of the electrons, which depends on $|\mathbf{E}_{\mathrm{SP}}|$, k_{SP}, and, most importantly, the angle, α, between the PE beam and the external SE. As the SEs are ejected as a cloud from the Au film, the 300 eV PE beams will simultaneously pass through this cloud of SE. With a 2 mm-diameter PE beam and low-energy SE, the effective PE–SE interaction time is 2–20 ns. This low-energy free electron–free electron scattering is a manifestation of Møller

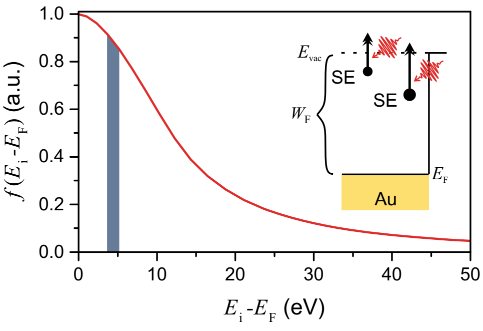

Fig. 4 Internal secondary electron (SE) energy spectrum for the Au film. $f(E_{\mathrm{i}} - E_{\mathrm{F}})$ is the normalized electron population at a given kinetic energy. The kinetic energy presented here is referenced to the Fermi energy, E_{F}. The shaded region indicates the population of electrons having energy between $E_{\mathrm{vac}} - h\nu$ and E_{vac}, where E_{vac} is the vacuum energy and $h\nu$ is the plasmon energy. Inset: schematic depiction of single-plasmon emission of internal SE by absorbing $h\nu = 1.55$ eV plasmons. Here, W_{F} is the Au work function.

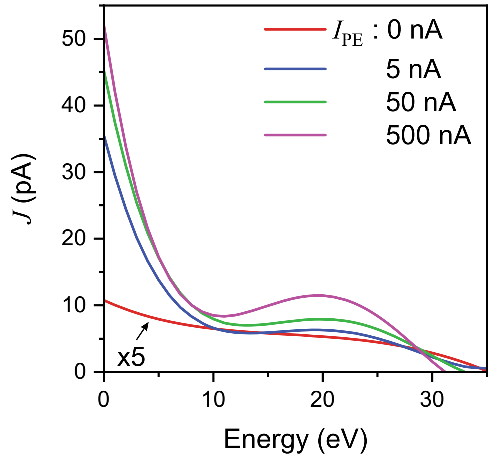

Fig. 5 Measured kinetic energy spectra at incident laser intensity, $I_{\mathrm{laser}} = 25$ GW cm^{-2} and $I_{\mathrm{PE}} = 0$, 5, 50, and 500 nA. It is noteworthy that the primary electron beam current, $I_{\mathrm{PE}} = 0$ nA (red) curve has been scaled by five times.

nonrelativistic scattering, in accordance with Mott[45], Klauber[46], and Williams et al.[47]. The key issue in the scattering process is the indistinguishability (i.e., their charge and mass are identical) of the two-electron system forming either a singlet or triplet state having antisymmetric and symmetric spin wave functions under interchange of the electrons, respectively. Accordingly, the spatial wave functions must be even or odd functions of the relative coordinates for the states of the two electrons, as this affects the scattering laws and thus alters the scattering cross-section when compared with Coulomb scattering. This scattering process is important in low-energy UEM, as it can alter the momentum and spatial distribution of the electrons leaving the sample.

The Møller nonrelativistic differential scattering cross-section is given by[47]:

$$\frac{d\sigma(\theta_s)}{d\Omega} = \left(\frac{q^2}{m_e V_R^2}\right)^2 \left(\begin{array}{c} \csc^{-4}(\theta_0/2) + \sec^{-4}(\theta_0/2) \\ -\left[\csc^{-2}(\theta_0/2)\sec^{-2}(\theta_0/2)\right] \\ \times \cos\left[\left(q^2/\hbar V_R^2\right)\log(\tan^2(\theta_0/2))\right] \end{array}\right) \times \frac{\left[\tan^2\psi + 2\tan\psi\sin\theta_0 + 1\right]^{3/2}}{1 - \tan\psi\sin\theta_0} \quad (1)$$

where q is the elementary electron charge, m_e is the electron mass, $\hbar$ is reduced Planck's constant, V_R is the relative velocity of the SE and PE, $\psi = (180° - \alpha)/2$, and θ_0 is the scattering angle in the center of mass frame (related to θ_s (see Fig. 1) through $\tan\theta_s = (\tan\psi - \sin\theta_0)\sec\theta_0$). For 300 eV PE and SE having kinetic energies up to 50 eV, $d\sigma(\theta_s)/d\Omega$ is highest in the direction normal to the Au film and drops off for decreasing θ_s (see Supplementary Note 6). Notably, the minimum cross-section occurs at $\theta_s = 26°$, indicating that the Møller nonrelativistic scattering of SE from the PE alone is not directly responsible for the observed 25°–30° beaming in the measured angular distribution (Fig. 2). However, there is a large cross-section in the direction parallel ($\theta_s = 0°$) to k_{SP} and the PE beam propagation direction. As these scattered SE are traveling almost perpendicular to the ponderomotive force from $\mathbf{E}_{SP}$, they will be affected by the $\mathbf{E}_{SP}$ more than any other SE. As a result, these SEs are accelerated and beamed by the SP wave.

Discussion

To fully model the experimental results, electron-tracking simulations were conducted (see Methods for a full description of the model). The model reproduces the experimental angular distribution at an $|\mathbf{E}_{SP}|$ of 17 V nm^{-1} (42 × peak electric field enhancement). When SEs are generated in the presence of $\mathbf{E}_{SP}$, the yield of external SE increases via single-plasmon absorption. Subsequently, due to Møller nonrelativistic scattering between SE and PE, those electrons that are scattered forward along the direction of propagation of the PE beam and k_{SP} spend more time interacting with $\mathbf{E}_{SP}$ and are deflected by the ponderomotive force. As depicted in Fig. 6, this interaction process is able to reproduce the experimentally observed 25° beaming and the increased cosine-like background distribution of SE. The background cosine-like distribution is due to the single-plasmon absorption that is responsible for the linear power scaling discussed earlier.

In summary, the experimental results presented here demonstrate the significant influence of an ultrafast SP field on externally injected electrons, specifically SEs. Single-plasmon absorption of internal SEs leads to a dramatic increase in the yield of SE as well as a marked increase in the number of low-energy electrons in the electron energy spectra. The SEs also undergo Møller nonrelativistic scattering from the PE beam that, in the presence of the high plasmonic field, gives rise to a distinct beaming in the angular distribution of the SEs. These results clearly indicate that SEs play a major role when studying low-energy ultrafast surface electron dynamics in the presence of high SP fields.

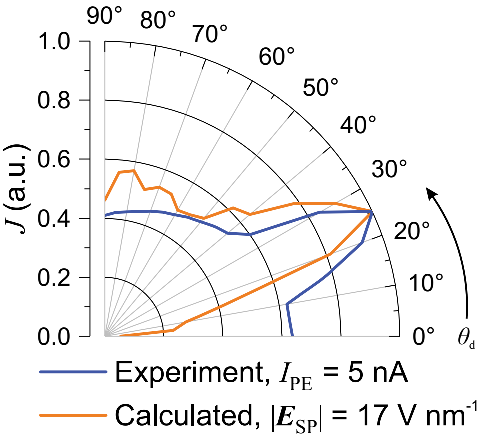

Fig. 6 Modelled angular distribution of total electron current. Calculated angular distribution (orange curve) of total electron current, J, compared with experimentally measured angular distribution (blue curve) at primary electron beam current, $I_{PE} = 5$ nA and peak surface plasmon electric field strength $|\mathbf{E}_{SP}| = 17$ V nm^{-1}.

Methods

Experimental setup. The 45 nm-thick Au film used in these experiments is deposited via magnetron sputtering on the hypotenuse side of a right-angle ultraviolet-fused silica prism. This sample was then placed in a vacuum chamber evacuated to 10^{-5} Torr for the duration of the experiment. Optical excitation of SPs is achieved by coupling 50 fs, 800 nm central wavelength, laser pulses at a 1 KHz repetition rate from a Ti:Sapphire chirped pulse amplifier to the 45 nm Au film via the Kretschmann geometry. The laser beam is collimated to a 4 mm beam waist to ensure the largest plasmon–electron interaction region. The 300 eV continuous electron beam is provided by a VG Electronics Leg 32 electron gun. To reduce charging, the Au film was grounded. The electrons are detected by a copper Faraday cup with a 5° acceptance angle mounted on an angular translation stage that is connected to a lock-in amplifier (Stanford Research SR830) taking its reference from an optical chopper (Stanford Research SR540) placed in the laser beam path. The use of a lock-in amplifier allows the detection of only those electrons that have interacted with the SP or incident laser field. Electron kinetic energy measurements are performed using a retarding potential analyzer.

Electron-tracking model. The electron-tracking simulation method is detailed elsewhere[48,49] with a detailed description in Supplementary Note 2. Briefly, to model the interaction of primary and SEs with the electromagnetic fields of $\mathbf{E}_{SP}$, electron-tracking code is implemented. The electromagnetic fields are calculated by solving the vectorial Maxwell's equations using the Yee-cell FDTD method[50] with Berenger perfectly matched layer boundary conditions[51]. Here, the SP fields are calculated for a 45 nm Au film excited with a 50 fs, $\lambda = 800$ nm laser pulse. By stepping in time through these fields, the electrons' trajectories are tracked in space and time via the nonrelativistic equation of motion $d\boldsymbol{v}/dt = q/m_e[\mathbf{E} + \boldsymbol{v} \times \mu\mathbf{H}]$, where q/m_e is the electron charge to mass ratio, $\mathbf{E}$ is the electric field, $\boldsymbol{v}$ is the electron velocity, and $\mathbf{H}$ is the magnetic field. The 300 eV PEs are placed between 0 and 50 nm above the Au surface with a velocity directed parallel to k_{SP} and released at random times to simulate a continuous electron beam. The external SE are given initial kinetic energy distribution $f(E_e) = (E_e - E_F - W_F)/(E_e - E_F)^4$, where E_e is the SE kinetic energy in vacuum[40] and is spatially directed in a cosine angular distribution.

Data availability

The data that support the findings of this study are available from the corresponding author upon reasonable request.

Received: 8 March 2019; Accepted: 13 January 2020;
Published online: 29 January 2020

References

1. Baum, P., Yang, D.-S. & Zewail, A. H. 4D visualization of transitional structures in phase transformations by electron diffraction. *Science* **318**, 788–92 (2007).

2. Kozák, M., Schönenberger, N. & Hommelhoff, P. Ponderomotive generation and detection of attosecond free-electron pulse trains. *Phys. Rev. Lett.* **120**, 103203 (2018).
3. Hassan, M. T., Baskin, J. S., Liao, B. & Zewail, A. H. High-temporal-resolution electron microscopy for imaging ultrafast electron dynamics. *Nat. Photonics* **11**, 425–430 (2017).
4. Hassan, M. T. Attomicroscopy: from femtosecond to attosecond electron microscopy. *J. Phys. B . Mol. Opt. Phys.* **51**, 032005 (2018).
5. Morimoto, Y. & Baum, P. Diffraction and microscopy with attosecond electron pulse trains. *Nat. Phys.* **14**, 252–256 (2018).
6. Siwick, B. J., Dwyer, J. R., Jordan, R. E. & Miller, R. J. D. An atomic-level view of melting using femtosecond electron diffraction. *Science* **302**, 1382–5 (2003).
7. Siwick, B. J., Dwyer, J. R., Jordan, R. E. & Miller, R. J. D. Femtosecond electron diffraction studies of strongly driven structural phase transitions. *Chem. Phys.* **299**, 285–305 (2004).
8. Grinolds, M. S., Lobastov, V. A., Weissenrieder, J. & Zewail, A. H. Four-dimensional ultrafast electron microscopy of phase transitions. *Proc. Natl Acad. Sci. USA* **103**, 18427–31 (2006).
9. Wall, S. et al. Atomistic picture of charge density wave formation at surfaces. *Phys. Rev. Lett.* **109**, 186101 (2012).
10. Vogelgesang, S. et al. Phase ordering of charge density waves traced by ultrafast low-energy electron diffraction. *Nat. Phys.* **14**, 184–190 (2017).
11. Carbone, F., Kwon, O.-H. & Zewail, A. H. Dynamics of chemical bonding mapped by energy-resolved 4D electron microscopy. *Science* **325**, 181–4 (2009).
12. Williamson, J. C. & Zewail, A. H. Structural femtochemistry: experimental methodology. *Proc. Natl Acad. Sci. USA* **88**, 5021–5 (1991).
13. Ihee, H. et al. Direct imaging of transient molecular structures with ultrafast diffraction. *Science* **291**, 458–62 (2001).
14. Hoegen, M. H. Ultrafast switching in an atomic wire system at surfaces. *MRS Bull.* **43**, 512–519 (2018).
15. Ruan, C.-Y., Vigliotti, F., Lobastov, V. A., Chen, S. & Zewail, A. H. Ultrafast electron crystallography: transient structures of molecules, surfaces, and phase transitions. *Proc. Natl Acad. Sci. USA* **101**, 1123–8 (2004).
16. Werner, W. S. M. et al. Contribution of surface plasmon decay to secondary electron emission from an Al surface. *Appl. Phys. Lett.* **99**, 184102 (2011).
17. Gulde, M. et al. Ultrafast low-energy electron diffraction in transmission resolves polymer/graphene superstructure dynamics. *Science* **345**, 200–4 (2014).
18. Müller, M., Paarmann, A. & Ernstorfer, R. Femtosecond electrons probing currents and atomic structure in nanomaterials. *Nat. Commun.* **5**, 5292 (2014).
19. Soriaga, M. P., Chen, X., Li, D. & Stickney, J. L. in *Encyclopedia of Inorganic Chemistry* (John Wiley & Sons, Ltd, New Jersey, 2008). https://doi.org/10.1002/0470862106.ia309.
20. Richardson, N. V. High resolution electron energy loss spectroscopy. *Curr. Opin. Solid State Mater. Sci.* **2**, 517–524 (1997).
21. Kesmodel, L. L. Applications of high-resolution electron energy loss spectroscopy to technical surfaces. *Langmuir* **14**, 1355–1360 (1998).
22. Erley, W., Ibach, H., Lehwald, S. & Wagner, H. CO vibrations on a stepped Ni surface. *Surf. Sci.* **83**, 585–598 (1979).
23. Formoso, V. et al. CO adsorption on Ni(1 0 0): Evidences for a weakly bound phase by HREELS measurements. *Surf. Sci.* **600**, 1456–1461 (2006).
24. von Schenck, H., Janin, E., Tjernberg, O., Svensson, M. & Göthelid, M. C. O. bonding on tin modified Pt(110)-(1×2). *Surf. Sci.* **526**, 184–192 (2003).
25. Rahman, T. S., Anton, A. B., Avery, N. R. & Weinberg, W. H. Electron-energy-loss spectroscopy of ordered oxygen overlayers on Ru(001). *Phys. Rev. Lett.* **51**, 1979–1982 (1983).
26. Bartolucci, F., Franchy, R., Barnard, J. C. & Palmer, R. E. Two Chemisorbed Species of O_2 on Ag(110). *Phys. Rev. Lett.* **80**, 5224–5227 (1998).
27. Wendt, S. et al. The interaction of water with silica thin films grown on Mo(1 1 2). *Surf. Sci.* **565**, 107–120 (2004).
28. Ibach, H. & Lehwald, S. The bonding of water molecules to platinum surfaces. *Surf. Sci.* **91**, 187–197 (1980).
29. Soto, J. E., Kim, Y.-G., Chen, X., Park, Y.-S. & Soriaga, M. P. Molecular chemisorption at well-defined Pd(111) electrode surfaces: hydroquinone sulfonate studied by UHV-EC-STM. *J. Electroanal. Chem.* **500**, 374–378 (2001).
30. Noh, J., Kato, H. S., Kawai, M. & Hara, M. Surface structure and interface dynamics of alkanethiol self-assembled monolayers on Au(111). *J. Phys. Chem. B* **110**, 2793–2797 (2006).
31. Duwez, A.-S., Yu, L. M., Riga, J., Pireaux, J.-J. & Delhalle, J. Molecular structure and surface order in monolayers of alkanethiols evidenced by HREELS. *Thin Solid Films* **327–329**, 156–160 (1998).
32. Zawadzka, J. A., Jaroszynski, D., Carey, J. & Wynne, K. Evanescent-wave acceleration of femtosecond electron bunches. *Nucl. Instrum. Methods Phys. Res. A Accel. Spectrom. Detect. Assoc. Equip.* **445**, 324–328 (2000).
33. Irvine, S. E., Dechant, A. & Elezzabi, A. Y. Generation of 0.4-keV Femtosecond electron pulses using impulsively excited surface plasmons. *Phys. Rev. Lett.* **93**, 184801 (2004).
34. Irvine, S. E. & Elezzabi, A. Y. Ponderomotive electron acceleration using surface plasmon waves excited with femtosecond laser pulses. *Appl. Phys. Lett.* **86**, 264102 (2005).
35. Kupersztych, J., Monchicourt, P. & Raynaud, M. Ponderomotive acceleration of photoelectrons in surface-plasmon-assisted multiphoton photoelectric emission. *Phys. Rev. Lett.* **86**, 5180–5183 (2001).
36. Nagel, P. M. et al. Surface plasmon assisted electron acceleration in photoemission from gold nanopillars. *Chem. Phys.* **414**, 106–111 (2013).
37. Dombi, P. et al. Ultrafast strong-field photoemission from plasmonic nanoparticles. *Nano Lett.* **13**, 674–678 (2013).
38. Petry, R. L. Secondary electron emission from tungsten, copper and gold. *Phys. Rev.* **28**, 362–366 (1926).
39. Greig, S. R., Morteza-Najarian, A., McCreery, R. L. & Elezzabi, A. Y. Surface plasmon driven lowering of the electron emission order in a carbon/gold bilayer film. *Appl. Phys. Lett.* **109**, 221104 (2016).
40. Seiler, H. Secondary electron emission in the scanning electron microscope. *J. Appl. Phys.* **54**, R1–R18 (1983).
41. Kanaya, K. & Kawakatsu, H. Secondary electron emission due to primary and backscattered electrons. *J. Phys. D. Appl. Phys.* **5**, 330 (1972).
42. Kaneko, T. Energy distribution of secondary electrons emitted from solid surfaces under electron bombardment: I. Theory. *Surf. Sci.* **237**, 327–336 (1990).
43. Lindhard, J. On the properties of a gas of charged particles. *Dan. Mat. Fys. Med.* **28**, 1–57 (1954).
44. Lindhard, J. & Winther, A. Stopping power of electron gas and equipartition rule. *Mat. Fys. Medd. Dan. Vid. Selsk.* **34**, 1–22 (1964).
45. Mott, N. F. The collision between two electrons. *Proc. R. Soc. A Math. Phys. Eng. Sci.* **126**, 259–267 (1930).
46. Klauber, R. D. in *Student Friendly Quantum Field Theory: Basic Principles and Quantum Electrodynamics* (Sandtrove Press, Iowa, 2014).
47. Williams, J. F. et al. Scattering of free electrons by free electrons. *Phys. Rev. A* **89**, 062717 (2014).
48. Greig, S. R. & Elezzabi, A. Y. Generation of attosecond electron packets via conical surface plasmon electron acceleration. *Sci. Rep.* **6**, 19056 (2016).
49. Greig, S. R. & Elezzabi, A. Y. On the role of terahertz field acceleration and beaming of surface plasmon generated ultrashort electron pulses. *Appl. Phys. Lett.* **105**, 041115 (2014).
50. Taflove, A. & Hagness, S. C. in *Computational Electrodynamics: The Finite-Difference Time-Domain Method* (Artech House, Massachusetts, 2000).
51. Bérenger, J.-P. Perfectly matched layer (PML) for computational electromagnetics. *Synth. Lect. Comput. Electromagn.* **2**, 1–117 (2007).

Acknowledgements

We are grateful to Professor Mark Stockman (Georgia State University), Professor Frank Meyer zu Heringdorf (University of Duisburg-Essen), Professor Norbert Kroó (Wigner Research Centre for Physics), Professor Cristian Denton (Universidad de Alicante), Dr. Nestor Arista (Centro Atomico Bariloche and Instituto Balseiro), and Professor James Williams (University of Western Australia) for their valuable and insightful discussions. This research was funded by the Natural Sciences and Engineering Research Council of Canada (NSERC).

Author contributions

S.R.G. and A.Y.E. conceived and planned the experiment, and wrote the main manuscript. S.R.G. performed the experiment, analyzed the data, performed the numerical simulations, and prepared the figures. J.B.K. helped with the analysis and discussion of the electron–plasmon interaction. A.Y.E. supervised the project. All authors reviewed the manuscript.

Competing interests

The authors declare no competing interests.

Additional information

Supplementary Information is available for this paper at https://doi.org/10.1038/s42005-020-0295-5.

Correspondence and requests for materials should be addressed to S.R.G.

Reprints and permission information is available at http://www.nature.com/reprints

Publisher's note Springer Nature remains neutral with regard to jurisdictional claims in published maps and institutional affiliations.

Open Access This article is licensed under a Creative Commons Attribution 4.0 International License, which permits use, sharing, adaptation, distribution and reproduction in any medium or format, as long as you give appropriate credit to the original author(s) and the source, provide a link to the Creative Commons license, and indicate if changes were made. The images or other third party material in this article are included in the article's Creative Commons license, unless indicated otherwise in a credit line to the material. If material is not included in the article's Creative Commons license and your intended use is not permitted by statutory regulation or exceeds the permitted use, you will need to obtain permission directly from the copyright holder. To view a copy of this license, visit http://creativecommons.org/licenses/by/4.0/.

© The Author(s) 2020